Quantum confinement and thickness-dependent electron transport in solution-processed In$_2$O$_3$ transistors

Ivan Isakov, Hendrik Faber, Alexander D. Mottram, Satyajit Das, Max Grell, Anna Regoutz, Rebecca Kilmurray, Martyn A. McLachlan, David J. Payne and Thomas D. Anthopoulos*

Dr. I. Isakov, Dr. A. D. Mottram, Dr. S. Das, M. Grell, Prof. T. D. Anthopoulos
Department of Physics and Centre for Plastic Electronics, Blackett Laboratory, Imperial College London, London SW7 2BW, UK.

Dr. A. Regoutz
Department of Chemistry, University College London, 20 Gordon Street, London WC1H 0AJ, UK

Dr. R. Kilmurray, Dr. M. A. McLachlan, Dr. D. Payne
Department of Materials, Royal School of Mines, Imperial College London, London SW7 2AZ, UK

Dr. H. Faber, Prof. T. D. Anthopoulos
King Abdullah University of Science and Technology (KAUST), KAUST Solar Center and Physical Science and Engineering Division (PSE), Thuwal, 23955-6900, Saudi Arabia
E-mail: thomas.anthopoulos@kaust.edu.sa

Abstract

The dependence of charge carrier mobility on semiconductor channel thickness in field-effect transistors is a universal phenomenon that has been studied extensively for various families of materials. Surprisingly, analogous studies involving metal oxide semiconductors are relatively scarce. Here, spray-deposited In$_2$O$_3$ layers are employed as the model semiconductor system to study the impact of layer thickness on quantum confinement and electron transport along the transistor channel. The results reveal an exponential increase of the in-plane electron mobility (μ_e) with increasing In$_2$O$_3$ thickness up to ≈10 nm, beyond which it plateaus at a maximum value of ≈35 cm^{2}V^{-1}s^{-1}. Optical spectroscopy measurements performed on the In$_2$O$_3$ layers reveal the emergence of quantum confinement for layers thickness <10 nm thick, which coincides with the thickness that μ_e starts deteriorating. By combining two- and four-probe field-effect mobility measurements with high-resolution atomic force microscopy, we show that the reduction in μ_e is attributed primarily to surface scattering. The study provides important guidelines for the design of next generation metal oxide TFTs.

Introduction

Low dimensional semiconducting systems have been developed for more than 30 years with numerous enabling applications in electronics, computing and sensing.[1-3] In recent years, the field started to shift from the high-end, high-cost deposition methods such as molecular beam epitaxy, metal-organic vapor phase epitaxy, and pulsed vapour deposition, to more cost-effective techniques, such as radio-frequency (RF) sputtering and solution-phase processing.[4, 5] Although RF sputtering offers scalable manufacturing, the growth of thin and uniform semiconducting layers and heterostructures with high enough precision and layer stoichiometry, remains challenging and hence costly.[6] On the other hand, recent progress in solution-phase processing of semiconductor films has allowed the deposition of ultra-thin layers (<10 nm) and the demonstration of numerous devices.[7-13] Despite the promise of scalable manufacturing, however, solution-based processing is often associated with the unintentional introduction of a high density of structural and chemical defects as compared to high-quality epitaxial layers. Therefore, an improved understanding of the relationship between the semiconductor's dimensionality and electronic properties is required.

A simple method for studying the electronic properties of semiconducting layers is via field-effect transistor measurements. Unfortunately, extrinsic device effects appear to often dominate the operating characteristics of such devices, making accurate determination of key material properties challenging.[14, 15] For instance, it has previously been shown that thin-film transistors (TFTs) based on different semiconductor materials exhibit a universal trait: the charge carrier mobility reduces with lowering channel thickness below a critical dimension.[16-23] This phenomenon applies to numerous established technologies including silicon-germanium transistors,[16] GaAs/AlGaAs quantum wells,[17] as well as emerging semiconductor technologies including two-dimensional (2D) materials (*e.g.* MoS_2),[18] organic semiconductors,[19-21] and metal oxide semiconductors.[22-24] Traditionally, the mobility-thickness relation has been used to distinguish between different carrier scattering mechanisms

provided one can control the layer thickness and uniformity with high enough accuracy. Based on such channel thickness-scaling studies, several different mechanisms have been proposed for the various semiconductor families, including Coulomb interaction scattering, phonon scattering, and surface roughness scattering (SRS). However, one materials family where the dependence of carrier mobility on the semiconductor layer thickness has yet to be thoroughly studied is that of the metal oxides.

Here we report on the impact of channel thickness variation on electron transport and optical properties of In_2O_3 layers grown via ultrasonic spray pyrolysis. We first establish that spray pyrolysis enables the growth of conformal In_2O_3 layers with thicknesses in the range ≈ 1 to 15 nm with a high degree of precision.[25, 26] Due to their low dimensionality, In_2O_3 layers exhibit quantum confinement accompanied by a pronounced thickness dependent electron mobility ranging from 10^{-3} to 35 cm^2 $V^{-1}s^{-1}$. To elucidate the origin of this dependence, we studied the evolution of electron transport, surface topography, optical properties, and electronic structure as a function of In_2O_3 layer thickness. Firstly, we eliminate those scattering mechanisms that cannot explain the experimentally observed trends. Secondly, we deduce the presence of quantum confinement in the thinnest layers by comparing our theoretical predictions with the experimentally measured thickness dependence of the energy bandgap (E_G) and valence band offset (VBO). Based on these results we conclude that the primary mechanism responsible for the dramatic electron mobility reduction in ultra-thin In_2O_3 channels is carrier surface scattering. The present study deepens our understanding of the electronic processes in metal oxides while provides valuable guidelines for the design of advanced metal oxide TFTs.

Results and Discussion

To study the dependence of electron transport as a function of In_2O_3 thickness, transistors with channel thickness ranging from ≈ 1 to ≈ 15 nm were fabricated via spray pyrolysis (see

Experimental for details). **Figure 1a** shows representative transfer characteristics for In_2O_3 transistors based on various channel thicknesses. Evidently, the channel on-current reduces in thinner channels and the switch-on voltage (V_{ON}) moves towards more positive gate bias (V_G), both indicative of a reduced carrier concentration. This dependence mirrors literature data on the thickness dependence of carrier transport for various types of transistors. [16, 18-20, 22] **Figure 1b** shows the calculated electron mobility (μ_e) obtained from several independent sets of In_2O_3 TFTs processed in the temperature range of 255-265 °C by different experimenters in our group. As can be seen, all batches exhibit similar trends characterized by a drastic mobility reduction from a maximum value of ≈ 35 cm^2 V^{-1}s^{-1} down to 10^{-3} cm^2 V^{-1}s^{-1} when the In_2O_3 layer thickness is reduced from 15 to ≈ 1 nm, respectively. A potential reason for this behaviour is the increase in the concentration of the deep trap states (or "tail" states), which are known to play a major role in polycrystalline systems such as solution-processed semiconductors.[27-29] It is known that the concentration of such defects might increase at the film surface due to the presence of dangling bonds, strain, diffusion of impurities, or adsorption of foreign chemical species.[30-32] As the surface of the layer comes closer to the electron transporting channel at the SiO_2/In_2O_3 interface, stronger interactions between the mobile electrons and the trap states/defect (scattering) should be expected. Other effects, such as changes in the layer microstructure with varying thicknesses and percolation effects, may also exist and contribute towards the observed phenomena. Considering these effects one could expect the energetic distribution of traps to differ as well.

To gain insight into the trap state distribution within the In_2O_3 layer, the analytical Grünewald model was employed to calculate the density of tail traps (trap DOS g_{BG}) in In_2O_3 layers with varying thickness.[33] In this method the DOS can be calculated directly from the transfer characteristics of the different In_2O_3 transistors and the obtained results are presented in **Figure 2a**. Evidently, the obtained data does not indicate any apparent increase in the trap DOS down to a layer thickness of ≈ 1.2 nm. On the basis of this analysis we may conclude that

deep trap states located on the surface of the layer cannot account for the dramatic mobility reduction seen in ultra-thin channels. The abrupt change seen in the trap DOS for ≈0.6 nm thick layers is most likely attributed to the discontinuity and limited surface coverage of the substrate by the In_2O_3 layer. Importantly, similar data are derived for transistors prepared in different batches, highlighting the reproducibility of the sample manufacturing but also the applicability of the analytical method employed (**Figure S1a**).

A further possible reason for the μ_e reduction observed is the presence of a high contact resistance (R_c). To remove possible R_c contributions, and thus to identify its role, if any, on the reduction of μ_e, 4-point probe (4pp) measurements were carried out (**Figure 2b**). As in the case of conventional 2-point probe (2pp) measurements, the 4pp method also reveals a significantly reduced μ_e for thinner films (≈7 nm) as compared to devices with thicker channel layers (≈ 15 nm). This suggests that the electron mobility reduction in thinner systems is an intrinsic feature of the In_2O_3 channel, *i.e.* not caused by high R_C, and does not depend on the measurement method. Direct comparison of the two methods reveals a slight increase in the 4pp-derived μ_e as compared to the 2pp method, extracted at similar bias (**Figure S2**).

Another mechanism that could potentially contribute to the deterioration of μ_e with reducing In_2O_3 layers thickness in **Figure 1b**, is variable phonon scattering.[34, 35] Strictly speaking, phonon scattering results in a mobility increase with lowering temperatures due to the phonon energy reduction. [36, 37] This, however, is not the case here as μ_e remains relatively constant between 300 K and 78 K (**Figure 2c** and **Figure S3**). Lastly, we also exclude Coulomb scattering as the dominant scattering mechanism since the latter would exhibit a much less sharp thickness-dependence carrier mobility than the one observed here (**Figure 1b**).[18] As an intermediate conclusion, the electrical measurements presented so far do not identify any clear mechanism that could account for the mobility reduction observed in ultra-thin channel In_2O_3 transistors.

In an effort to improve our understanding of the system behaviour, we investigated the valence band (VB) and conduction band (CB) positions of the layers using complementary optical and structural characterisation methods. First, the optical E_G of In_2O_3 layers was measured using variable-angle spectroscopic ellipsometry (VASE). The characteristic Tauc plots were obtained from fitting the optical constants n and k to the ellipsometry data (**Figure S4**). Since the fitting results depend significantly on the choice of the physical model, several models were used for the bandgap estimation. The difference in the calculated bandgap (and equally the extracted film thickness) across the different models is translated into the value error shown in **Figure 3a**. Evidently, the E_G increases dramatically in thinner In_2O_3 layers, rising from 3.3 eV (9.5 nm) up to 3.7 eV (3 nm). This characteristic increase in bandgap is usually explained by quantum confinement occurring at layer thicknesses that are comparable to de Broglie wavelength in the semiconductor material. Often, however, solution-processed layers do not exhibit this behaviour due to their poor layer uniformity, with a few exceptions.[9, 38, 39]

To further validate the energy quantization effect in our spray-coated In_2O_3 layers, we conducted X-ray photoelectron spectroscopy (XPS) measurements and the results are shown in **Figure S5**. XPS is an accurate method to measure the valence band maximum (VBM) position relative to the Fermi energy (E_F) of a material. Similar to the increase in optical bandgap, an increase in the valence band offset of 0.3 eV was found between the thickest and thinnest In_2O_3 layers. Additionally, XPS measurements of several In_2O_3 samples showed a noticeable Fermi level (E_F) edge in their spectra (**Figure S5a** and **Figure S5c**). This indicates that some states in the conduction band are filled, meaning that the electronic bandgap can be calculated as the difference between E_F and the VBM. This calculation puts the electronic E_G in the range of 2.6-2.9 eV, which is significantly smaller than the optical E_G values determined using VASE (3.3-3.7 eV) in **Figure 3a**. This discrepancy, however, has been observed before in In_2O_3 and was attributed to the special feature of its band diagram.[40, 41] The electronic band structure of In_2O_3 is known for its fundamental bandgap of 2.7-2.9 eV with a forbidden transition between the CB

and VB, and an allowed indirect optical bandgap around 3.7 eV.[41] These values are in line with our current observations.

We have measured the CB offset (the difference between E_F and the CB edge E_C) in In$_2$O$_3$ films by considering the conventional semiconductor model for charge transport and carrier concentration.[37] Since the Al/In$_2$O$_3$ contact resistance in our samples is found to be negligible, the conductivity (σ) due to the unipolar electron transport in the channel, at $V_G = 0$ V, can be estimated and subsequently used to determine the carrier concentration (N_e) using:

$$\sigma = \mu_e \, N_e e \tag{1}$$

$$N_e = \sigma / \mu_e e \tag{2}$$

where μ_e is the electron carrier mobility inferred from the field-effect measurements and e the electron charge (see **Figure S6**). The evolution of N_e as a function of In$_2$O$_3$ layer thickness is presented in **Figure 3b**. Here it may be argued that estimating N_e using the conductivity equation may not be precise. To address this point, we performed Hall Effect measurements on a 12 nm thick layer of In$_2$O$_3$ to confirm the magnitude of N_e. The open red circle in **Figure 3b** shows the N_e value obtained from this measurement and is in good agreement with the value of N_e obtained from TFT measurements for a similar thickness sample. Use of thinner samples, did not allow meaningful Hall Effect measurements due to their high resistance and thus were not included in this study.

By considering the Fermi-Dirac distribution of electrons and the DOS within the CB and assuming negligible tail states (see *Supporting Information*),[37] we were able to estimate the CB offset. The calculated values are shown in **Figure 3c**, where the plot of the E_F-E_C *versus* thickness follows a familiar increase of the band offset in thinner films due to quantum confinement. For illustration purposes, **Figure S7** also depicts the thickness dependence of the bandgap change (ΔE_G) and change in valence band offset (ΔE_F-E_V) due to energy quantization, based on ellipsometry and XPS measurements, respectively. In both cases, ΔE is computed as the difference between the respective energy value and a reference energy value which in this

case is the value measured for the thickest In_2O_3 sample (bulk). Noticeably, all datasets show a similar increase by a value of 0.3-0.5 eV for the layer thickness of around 3 nm. The solid line in **Figure 3c** shows the energy shift due to quantum confinement calculated for spray deposited ultra-thin In_2O_3 layers:

$$\Delta E = h^2/(8m^*W)^2, \tag{3}$$

where W is the layer thickness, h is Planck's constant, and m^* is the effective mass for electrons ($m^*_e = 0.3$) and holes ($m^*_h = 0.6$).[9, 42, 43] As evident from **Figure 3**, the calculated and measured data are in good agreement, thus corroborating each other and undoubtedly indicating the existence of quantum confinement in ultrathin In_2O_3 layers.

For ultra-thin semiconducting layers with a non-negligible thickness variation, such as the present In_2O_3 layers, the phenomenon of quantum confinement translates into a variable potential landscape, *i.e.* the bandgap energy and E_C change locally due to layer thickness variation. These energy fluctuations can, under certain circumstances, be seen as scattering centres that impede charge carrier transport. The latter scattering mechanism is called surface roughness scattering (SRS).[17, 44] In the case of our ultra-thin In_2O_3 layers (≤ 10 nm), the root mean square (RMS) surface roughness measured via atomic force microscopy (AFM) is found to vary between ≈ 1 and 2.5 nm (**Figure 4a** and **Figure S8**). Interestingly, the RMS roughness increases linearly with increasing layer thickness and despite the low values, it becomes comparable with the overall In_2O_3 thicknesses (when $W \leq 10$ nm). In the case of a thin transistor channels such significant layer thickness fluctuations (Δ) could alter the electrostatic landscape and lead to surface carrier scattering.

The common SRS model assumes a magnitude of thickness fluctuations, Δ, that is independent of the layer thickness, W, and manifests itself in the following dependence of carrier mobility, μ_e:[17, 44]

$$\mu_e \approx \frac{W^6}{\Delta^2}. \tag{4}$$

In the case of In_2O_3 layers grown by spray pyrolysis, the experimentally determined Δ depends linearly on W (**Figure 4a** and **Figure S8a**), and for $W < 8$ nm the two parameters become comparable ($\Delta \approx W$) and **Eq. 4** becomes:

$$\mu_e \approx \frac{W^6}{W^2} = W^4. \tag{5}$$

The experimentally determined μ_e dependence on In_2O_3 thickness is plotted in **Figure 4b** (symbols), together with both the conventional ($\propto W^4$) and adjusted ($\propto W^6$) SRS models (solid lines). While the common SRS model fails to describe our experimental results, the adjusted power-law prediction of **Eq. 5** is in excellent agreement. Out of all the potential scattering mechanisms, only the surface roughness scattering with thickness-dependent roughness was able to explain the experimental observations. We therefore conclude that SRS is the dominant mechanism responsible for the electron mobility deterioration with reduced channel thickness (**Figure 1b**).

Figure 5 provides a schematic illustration of the relation between Δ and W (**Figure 5a-b**) and the impact on the potential landscape for a thin and a thick In_2O_3 layer (**Figure 5c-d**). The quantum confinement leads to a variable potential landscape (ΔE_G), *i.e.* the energy fluctuates locally depending on the surface roughness. The effect is more pronounced in thinner layers where the strong surface roughness fluctuations act as scattering points which ultimately dominate long range electron transport. Our results indicate, among other things, that reducing the surface roughness of ultra-thin solution-processed metal oxide semiconductor layers could allow for a further increase of the electron field-effect mobility in next generation metal oxide TFTs.

Conclusion

We reported the first systematic study of the influence of semiconductor channel thickness on electron transport in In_2O_3 TFTs prepared by ambient ultrasonic spray pyrolysis. We discover

that spray deposited In_2O_3 layers exhibit quantum confinement when their thickness becomes less than 10 nm. The electron mobility was also found to be strongly dependent on film thickness and deteriorates exponentially with reducing layer thickness below a critical value of 10 nm. The latter phenomenon was successfully explained by invoking a surface roughness scattering model. The work advances our understanding of the electronic transport processes in solution-grown metal oxide semiconductors and could prove critical for the development of metal oxide TFTs that rely on the use of ultra-thin semiconducting channels/layers.

Experimental

Transistor fabrication: The TFTs were fabricated on degenerately doped silicon substrates with thermally grown silicon oxide of 100 nm thickness. The precursor solution was prepared by mixing $In(NO_3)_3 \cdot H_2O$ (Indium Corporation, 5N (99.999%) powder with DI water at a concentration 30 mg mL^{-1}. In_2O_3 thin films were deposited using a SonoTek ultrasonic spray pyrolysis system at substrate temperatures between 255 and 265 °C. The films were deposited by repeated passes of the spray nozzle over the substrate where the substrate surface is covered with a fine mist of the precursor solution. Different thicknesses of the final solid film can be achieved by variation of the number of passes made in the process. This is also referred to as the number of layers within this manuscript. For additional details of the methodology for In_2O_3 TFT fabrication please refer to our previous publication.[25] It was shown previously that the mechanism for film growth is governed by the Leidenfrost effect dominated boiling and that it allows high crystallinity and smoothness of the films.[26] The thickness of the films ranged between 1.5 nm and 15 nm and was measured using atomic force microscopy (AFM) and spectroscopic ellipsometry (see **Figure S9** and **Figure S10**). Drain-source contacts were deposited by thermal evaporation of aluminium through a shadow mask. Unless otherwise specified, the TFT channel width was 1 mm and the channel length was 100 μm. For the 4-point probe method, the films were patterned using conventional photolithography

(MICROPOSIT S1813 photoresist, 115 °C baking, standard MICROPOSIT remover, In_2O_3 etching in diluted HCl, and residual photoresist removal in acetone). The metal contacts were patterned using lift-off photolithography using the following steps: 1. Spin-coating of MicroChem LOR A photoresist and baking at 150 °C, 2. second layer deposition: MICROPOSIT S1813 photoresist and baking at 115 °C, 3. UV exposure through a metal mask, 4. removal of an un-exposed LOR photoresist/microposit photoresist and creating an undercut in isopropyl alcohol, 5. vacuum deposition of Al over the whole sample, 6. removing of photoresist and lifting-off metal using MicroChem's Remover 1165. An example of a patterned device is shown in **Figure S2** and the schematic fabrication process is shown in **Figure S11**.

Grünewald method: In this work we use an analysis scheme that allows the calculation of the trap states below a mobility band edge from a single transfer characteristic measurement, as first published by Grünewald *et al.*[33] A qualitative explanation of the fundamental theory behind this scheme is that states below the bandgap slow the progression of the quasi-Fermi level towards the conduction band. These bandgap states retard the filling of the conduction band, hence altering the subthreshold slope of the TFT. The details for the Grünewald analysis scheme can be found in **Supporting Note 1** in the *Supporting information.*

Ellipsometry: Variable angle spectroscopic ellipsometry measurements were carried out on a J.A. Woollam ellipsometer. The films were prepared in the identical process to those measured electronically. Ellipsometric angles were measured at photon energies between 1.3 and 4.1 eV in a reflection mode. Measurements were performed at 65°, 70° and 75° incidence angles. Measurement data was analysed using the WVASE32 software package. Si/SiO_2 reference samples without In2O3 films atop were measured under the same conditions to verify the SiO_2 thickness of the substrates.

X-ray photoelectron spectroscopy (XPS): The XP spectra were recorded on a Thermo Scientific K-Alpha+ X-ray photoelectron spectrometer operating at 2×10^{-9} mbar base pressure. This

system incorporates a monochromated, microfocused Al Ka X-ray source ($hv = 1486.6$ eV) and a 180° double focusing hemispherical analyser with a 2D detector. Valence band spectra were collected at 15 eV pass energy using an X-ray spot size of 400 μm. All data were analysed using the Avantage software package.

Supporting Information
Supporting Information is available from the Wiley Online Library or from the author.

References

[1] M. Chhowalla, D. Jena, H. Zhang, *Nat. Rev. Mater.* **2016**, 1, 1.
[2] S. Das, V. Jayaraman, *Prog. Mater. Sci.* **2014**, 66, 112.
[3] G. C. Papavassiliou, *Prog. Solid State Ch.* **1997**, 25, 125.
[4] K. Nomura, H. Ohta, A. Takagi, T. Kamiya, M. Hirano, H. Hosono, *Nature* **2004**, 432, 488.
[5] B. A. Ridley, *Science* **1999**, 286, 746.
[6] K. Abe, K. Nomura, T. Kamiya, H. Hosono, *Phys Rev B* **2012**, 86, 081202(R).
[7] A. R. Kirmani, E. F. Roe, C. M. Stafford, L. J. Richter, *Materials Advances* **2020**, 1, 167.
[8] Y.-H. Lin, H. Faber, K. Zhao, Q. Wang, A. Amassian, M. McLachlan, T. D. Anthopoulos, *Adv. Mater.* **2013**, 25, 4340.
[9] J. G. Labram, Y.-H. Lin, K. Zhao, R. Li, S. R. Thomas, J. Semple, M. Androulidaki, L. Sygellou, M. McLachlan, E. Stratakis, A. Amassian, T. D. Anthopoulos, *Adv. Funct. Mater.* **2015**, 25, 1727.
[10] D. Khim, Y. H. Lin, T. D. Anthopoulos, *Adv. Funct. Mater.* **2019**, 29, 1902591.
[11] M. Lee, J. W. Jo, Y. J. Kim, S. Choi, S. M. Kwon, S. P. Jeon, A. Facchetti, Y. H. Kim, S. K. Park, *Adv. Mater.* **2018**, 30.
[12] Y. S. Rim, H. Chen, X. Kou, H. S. Duan, H. Zhou, M. Cai, H. J. Kim, Y. Yang, *Adv. Mater.* **2014**, 26, 4273.
[13] K. Tetzner, I. Isakov, A. Regoutz, D. J. Payne, T. D. Anthopoulos, *J. Mater. Chem. C* **2017**, 5, 59.
[14] A. F. Paterson, S. Singh, K. J. Fallon, T. Hodsden, Y. Han, B. C. Schroeder, H. Bronstein, M. Heeney, I. McCulloch, T. D. Anthopoulos, *Adv. Mater.* **2018**, 30, 1801079.
[15] J. F. Wager, *J. Soc. Inf. Disp.* **2010**, 18, 749.

[16]   C. N. Chleirigh, N. D. Theodore, H. Fukuyama, S. Mure, H. U. Ehrke, A. Domenicucci, J. L. Hoyt, *IEEE Trans. Electron Devices* **2008**, 55, 2687.

[17]   H. Sakaki, T. Noda, K. Hirakawa, M. Tanaka, T. Matsusue, *Appl. Phys. Lett.* **1987**, 51, 1934.

[18]   S.-L. Li, K. Wakabayashi, Y. Xu, S. Nakaharai, K. Komatsu, W.-W. Li, Y.-F. Lin, A. Aparecido-Ferreira, K. Tsukagoshi, *Nano Lett.* **2013**, 13, 3546.

[19]   R. Ruiz, A. Papadimitratos, A. C. Mayer, G. G. Malliaras, *Adv. Mater.* **2005**, 17, 1795.

[20]   F. Dinelli, M. Murgia, P. Levy, M. Cavallini, F. Biscarini, D. M. de Leeuw, *Phys. Rev. Lett.* **2004**, 92, 116802.

[21]   H. Xu, W.-J. Zhai, C. Tang, S.-Y. Qiu, R.-L. Liu, Z. Rong, Z.-Q. Pang, B. Jiang, J. Xiao, C. Zhong, B.-X. Mi, Q.-L. Fan, W. Huang, *J. Phys. Chem. C* **2016**, 120, 17184.

[22]   L. Shao, K. Nomura, T. Kamiya, H. Hosono, *Electrochem. Solid-State Lett.* **2011**, 14, H197.

[23]   S. Major, A. Banerjee, K. L. Chopra, K. C. Nagpal, *Thin Solid Films* **1986**, 143, 19.

[24]   M. Ortel, S. Pittner, V. Wagner, *J. Appl. Phys.* **2013**, 113, 154502.

[25]   H. Faber, Y.-H. Lin, S. R. Thomas, K. Zhao, N. Pliatsikas, M. A. McLachlan, A. Amassian, P. A. Patsalas, T. D. Anthopoulos, *ACS Appl. Mater. Interfaces* **2014**, 7, 782.

[26]   I. Isakov, H. Faber, M. Grell, G. Wyatt-Moon, N. Pliatsikas, T. Kehagias, G. P. Dimitrakopulos, P. P. Patsalas, R. Li, T. D. Anthopoulos, *Adv. Funct. Mater.* **2017**, 27, 1606407.

[27]   S. Lee, K. Ghaffarzadeh, A. Nathan, J. Robertson, S. Jeon, C. Kim, I. H. Song, U. I. Chung, *Appl. Phys. Lett.* **2011**, 98, 203508.

[28]   F. Torricelli, J. R. Meijboom, E. Smits, A. K. Tripathi, M. Ferroni, S. Federici, G. H. Gelinck, L. Colalongo, Z. M. Kovacs-Vajna, D. de Leeuw, E. Cantatore, *IEEE Trans. Electron Devices* **2011**, 58, 2610.

[29]   A. Zeumault, V. Subramanian, *Adv. Funct. Mater.* **2016**, 26, 955.

[30]   B. L. Zhang, H. Li, X. J. Zhang, Y. Luo, Q. P. Wang, A. M. Song, *Appl. Phys. Lett.* **2015**, 106, 093506.

[31]   J. K. Jeong, H. W. Yang, J. H. Jeong, Y. G. Mo, H. D. Kim, *Appl. Phys. Lett.* **2008**, 93, 123508.

[32]   Z. Zhang, J. T. Yates, *Chem Rev* **2012**, 112, 5520.

[33]   M. Grünewald, P. Thomas, D. Würtz, *Phys. Status Solidi B* **1980**, 100, K139.

[34]   P. J. Price, *Ann. Phys. (N Y)* **1981**, 133, 217.

[35]   E. H. Hwang, S. Das Sarma, *Phys Rev B* **2008**, 77, 115449.

[36]   S. I. Takagi, J. L. Hoyt, J. J. Welser, J. F. Gibbons, *J. Appl. Phys.* **1996**, 80, 1567.

[37]   S. M. Sze, K. K. Ng, *Physics of Semiconductor Devices*, John Wiley & Sons, Inc., 2006.

[38]   J. G. Labram, N. D. Treat, Y. H. Lin, C. H. Burgess, M. A. McLachlan, T. D. Anthopoulos, *Adv. Funct. Mater.* **2016**, 26, 1656.

[39]   Y. H. Lin, H. Faber, J. G. Labram, E. Stratakis, L. Sygellou, E. Kymakis, N. A. Hastas, R. P. Li, K. Zhao, A. Amassian, N. D. Treat, M. McLachlan, T. D. Anthopoulos, *Adv. Sci.* **2015**, 2, 1500058.

[40]   A. Walsh, J. L. F. Da Silva, S. H. Wei, C. Korber, A. Klein, L. F. J. Piper, A. DeMasi, K. E. Smith, G. Panaccione, P. Torelli, D. J. Payne, A. Bourlange, R. G. Egdell, *Phys. Rev. Lett.* **2008**, 100, 167402.

[41]   P. D. C. King, T. D. Veal, D. J. Payne, A. Bourlange, R. G. Egdell, C. F. McConville, *Phys. Rev. Lett.* **2008**, 101, 116808.

[42]   N. Preissler, O. Bierwagen, A. T. Ramu, J. S. Speck, *Phys Rev B* **2013**, 88, 085305.

[43]   M. Fox, R. Ispasoiu, *Quantum Wells, Superlattices, and Band-Gap Engineering. In: Kasap S., Capper P. (eds) Springer Handbook of Electronic and Photonic Materials*, Springer, Boston, MA, 2006.

[44]   T. Ando, A. B. Fowler, F. Stern, *Rev. Mod. Phys.* **1982**, 54, 437.
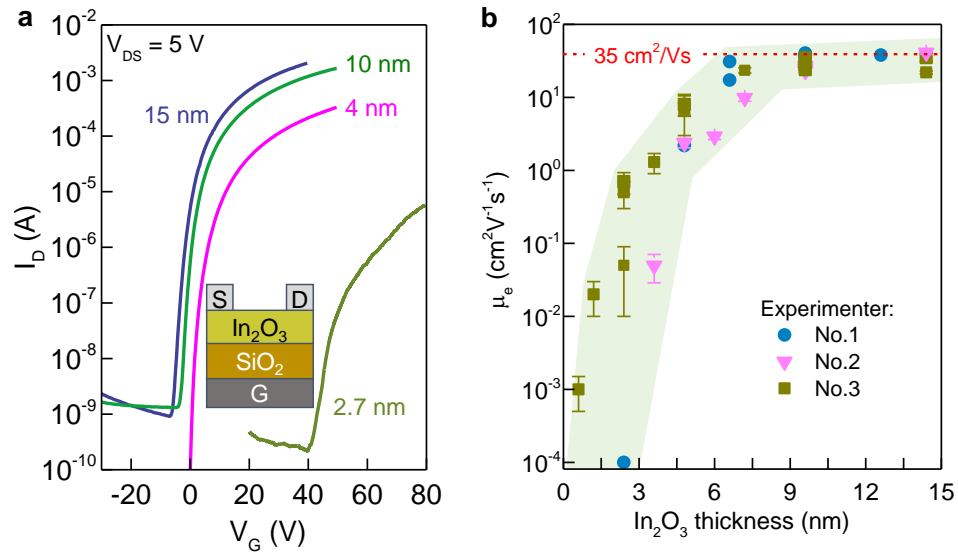
Figures

Figure 1. (a) Transfer characteristics for In_2O_3 transistors based on different channel thicknesses between 2.7 and 15 nm. The channel width and length for all TFTs were 1 mm and 80 µm, respectively. The inset shows the schematic of the bottom-gate, top-contact TFT architecture employed. (b) Channel thickness dependence of the carrier mobility gathered by three different experimenters.
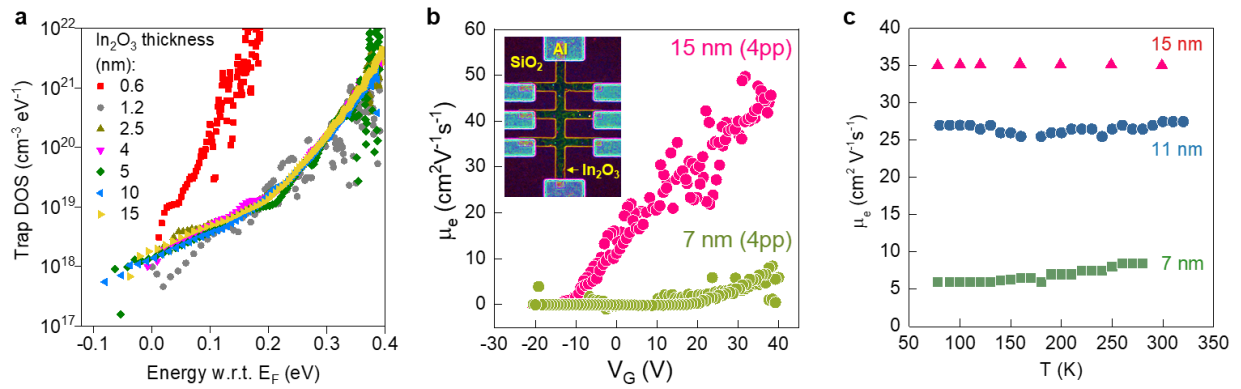
Figure 2. (a) Density of tail trap states of sample sets with channel thicknesses between 0.6 and 15 nm, prepared at 255 °C. (b) Carrier mobility for samples with two different thicknesses, acquired using a four-point-probe (4pp) measurement. The inset shows the image of a patterned In_2O_3 thin film used for the (4pp) method (c) Temperature dependence of charge carrier mobility of In_2O_3 thin films of different thicknesses.
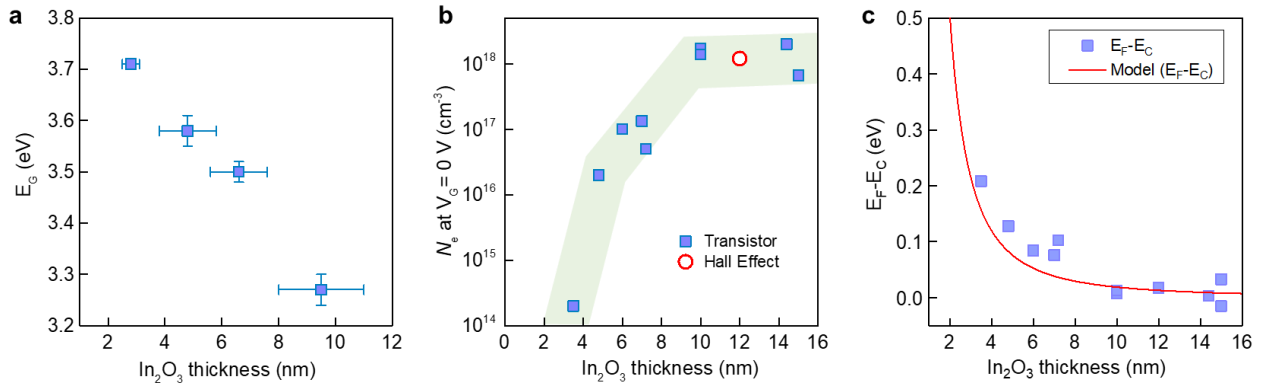
Figure 3. (a) Optical bandgap (E_G) derived from the Tauc plots (see *Supplementary Information*). (b) Carrier concentration (N_e) derived from the transistor transfer curves (solid squares) and Hall Effect measurement (open circle). (c) Thickness dependence of the change in the conduction band offset (E_F-E_C) for In_2O_3 layers. The solid line is a theoretical calculation for the energy shifts due to quantum confinement calculated using equation (3) and the effective electron mass
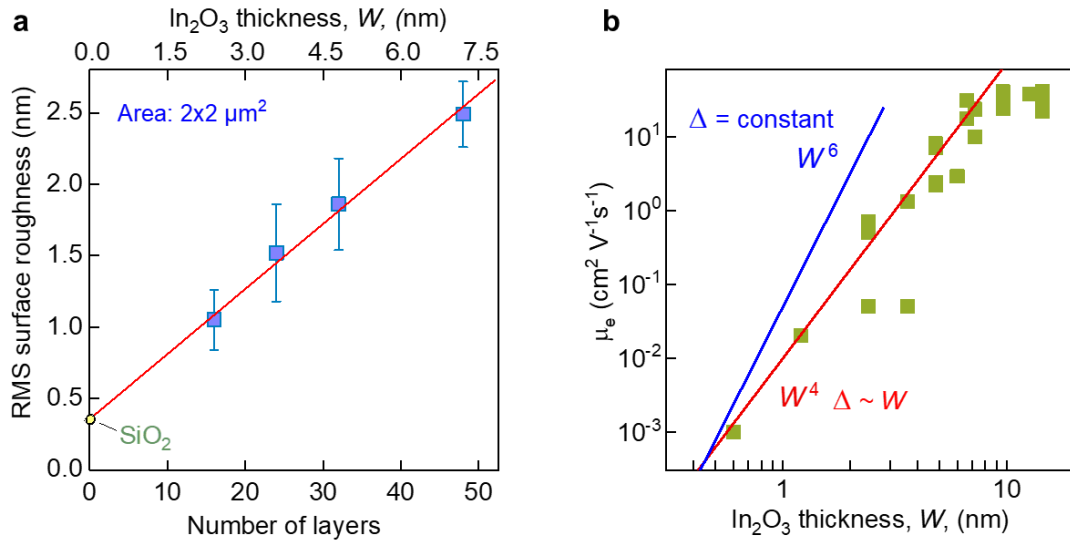
Figure 4. (a) RMS surface roughness calculated from the AFM data for In_2O_3 layers of varying thickness (see Figure S8). (b) Logarithmic representation of the electron mobility (μ_e) dependence on In_2O_3 layer thickness (symbols). The two solid lines represent fittings to the common surface roughness scattering model (blue line $\approx W^6$) and the modified model red line ($\approx W^4$).
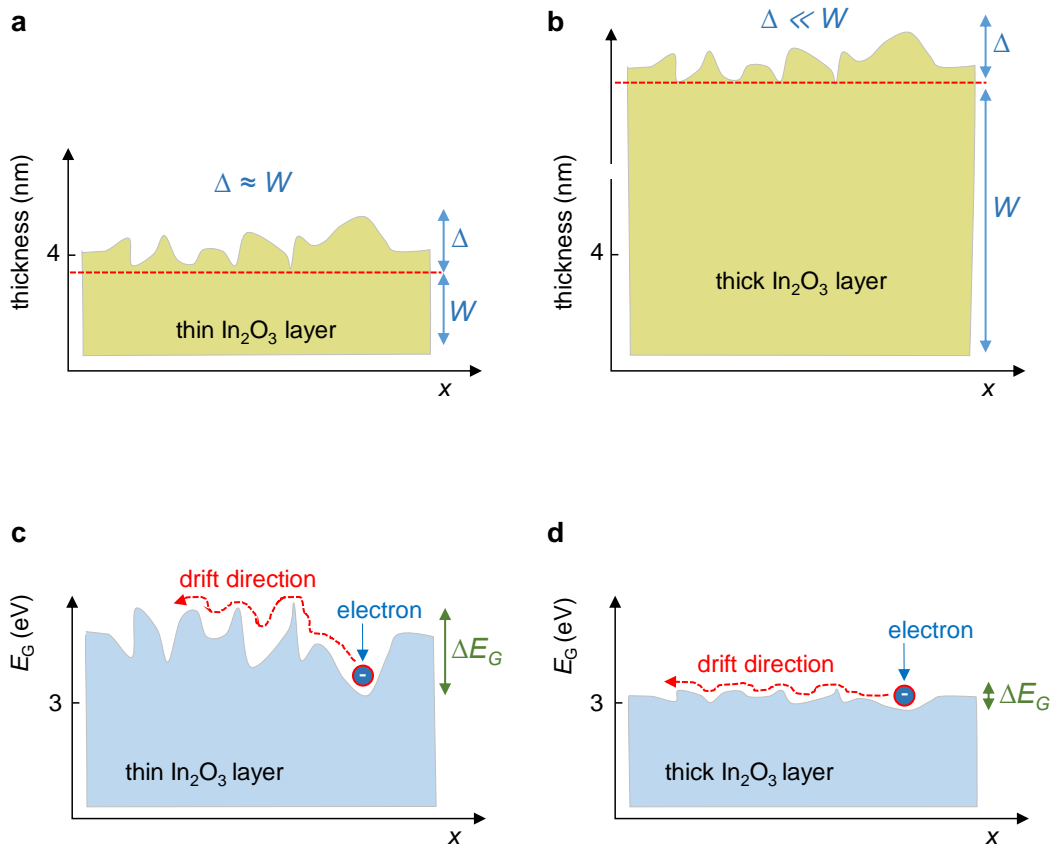
Figure 5. Schematics illustrating the surface roughness scattering effect in thin semiconducting films. Schematic cross-sectional view of a thin (a) and a thick (b) In_2O_3 layer with comparable surface roughness fluctuations (Δ). (c) Schematic depiction of the combined effect of quantum confinement and Δ in ultra-thin In_2O_3 layers and the creation of scattering centres due to the presence of a disordered potential landscape. (d) For thicker In_2O_3 layers the surface roughness induces only a small E_G fluctuation, due to the absence of energy quantization, with a minimum impact on electron transport in the channel.

ToC Entry Text

The electron mobility in In_2O_3 transistors fabricated via spray pyrolysis decreases with reduced channel thickness. Evidence for quantum confinement in these ultra-thin layers is gathered and the dramatic mobility decrease is correlated to the In_2O_3 surface topography and explained by invoking a modified surface roughness scattering carrier model.

Keyword indium oxide, spray pyrolysis, quantum confinement, surface roughness scattering, thin-film transistor

Ivan Isakov, Hendrik Faber, Alexander D. Mottram, Satyajit Das, Max Grell, Anna Regoutz, Rebecca Kilmurray, Martyn A. McLachlan, David J. Payne and Thomas D. Anthopoulos*

Quantum confinement and thickness-dependent electron transport in solution-processed In_2O_3 transistors
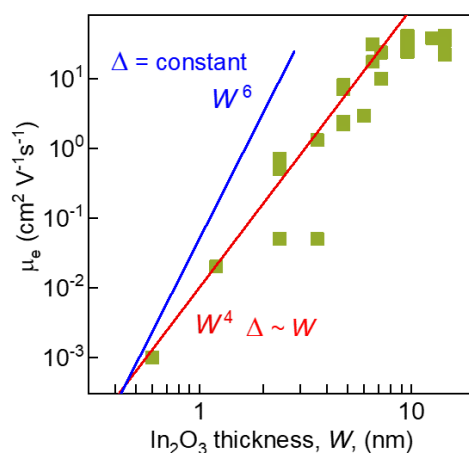
Supporting Information

Quantum confinement and thickness-dependent electron transport in solution-processed In2O3 transistors

Ivan Isakov, Hendrik Faber, Alexander D. Mottram, Satyajit Das, Max Grell, Anna Regoutz, Rebecca Kilmurray, Martyn A. McLachlan, David J. Payne and Thomas D. Anthopoulos*

Supporting Note 1: Grünewald analysis

To start with a field-effect voltage (V_F) is defined such that at $V_F = 0$ the TFT is at flat-band voltage. Since the flat-band of a TFT coincides with the turn-on voltage (V_{on}), the field-effect voltage is related to the applied gate voltage (V_G) by $V_F = V_G - V_{on}$. The first relationship of the analysis scheme is between the density of charge carriers at the semiconductor/dielectric interface ($n_0(\phi_0(V_F))$) and the internal potential at the interface ($\phi_0(V_F)$):

$$n_0(\phi_0(V_F)) = \frac{I_{off}C_{ins}}{qt_{sc}}\left(\frac{dI_D(V_F)}{dV_F}\right)^{-1}\left(e^{\beta\phi_0(V_F)} - 1\right). \qquad \text{(ES1)}$$

where I_{off}, C_{ins}, t_{sc} and q are the off-current, geometric capacitance, thickness of the semiconductor and elementary charge in turn, $\beta = 1/k_BT$ where k_B is the Boltzmann constant and T is the temperature and finally I_D is the drain current. Equation (ES1) cannot be solved without a relationship between the internal potential at the interface and the applied gate voltage. To calculate this, there is a second relationship:

$$\frac{C_{ins}t_{sc}}{I_{off}\varepsilon_{sc}k_BT}\left[V_FI_D(V_F) - \int_0^{V_F}I_D(V_F)\mathrm{d}V_F\right] = e^{\phi_0(V_F)\beta} - \beta\phi_0(V_F) - 1 \qquad \text{(ES2)}$$

where ε_{sc} is the permittivity of the semiconductor. Equation (S2) must be numerically solved for every experimental value of V_F which can then be reinserted into Equation (ES1) to calculate $n_0(\phi_0(V_F))$.

Finally, to calculate the DOS of bandgap states (g_{BG}), it is important to know that the density of charge carriers is the convolution of the total density of states both in the bandgap and in the conduction band, with the Fermi function. Therefore, a deconvolution of the density of charge carriers with respect to the Fermi function is required. The simplest way to perform this is by making the often used zero temperature approximation[1] that turns the Fermi function into a Heaviside function, and from this the deconvolution becomes:

$$g_{BG}(\phi_0) = \frac{\mathrm{d}n_0}{\mathrm{d}\phi_0}. \qquad \text{(ES3)}$$

During the derivations of Equations (ES1) and (ES2) an important assumption is made, which is that the semiconductor films being analysed is thick enough that the electric field tends to zero smoothly at the semiconductor surface. This is the thick film approximation for which there is no definite depth at which it breaks down. Simple calculations based on the work by Skinner[2] show that at 5 nm the electric field and charge distributions within the semiconductor remains equivalent with or without the thick film approximation.

SI Figures
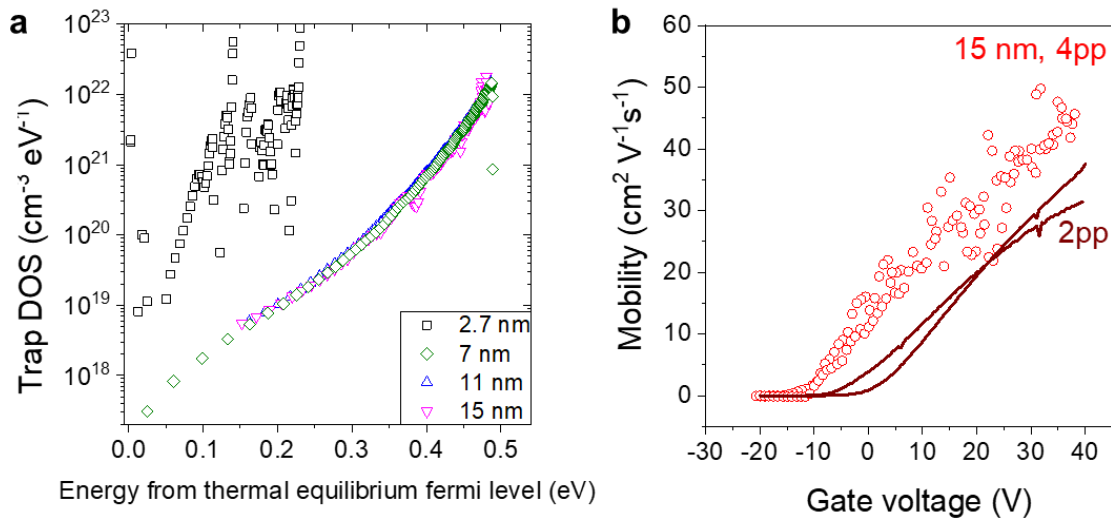
Figure S1. (a) Results of a Grünewald analysis of a different batch of samples compared to the one in the main text prepared at 265 °C, showing repeatability of the experiment (compare with **Figure 2a**). (b) Comparison between two-point probe (2pp) and four-point probe (4pp) method for measuring carrier mobility, showing slight increase in the mobility calculated by 4pp method.
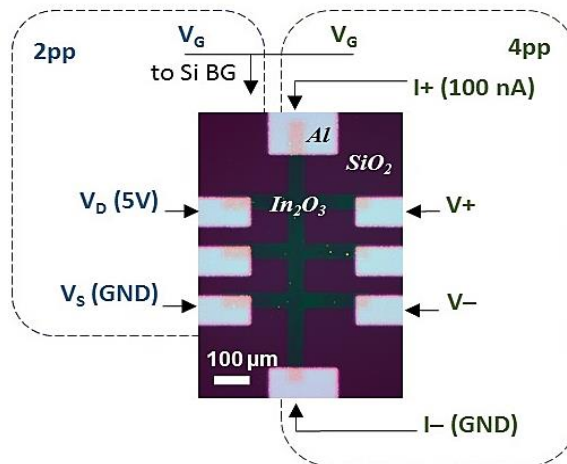

Figure S2. Optical image of a patterned In_2O_3 thin film used for mobility measurements via two-point probe (2pp) and four-point probe (4pp) method, respectively. The surrounding schematics indicate the electrical connections used for either case.
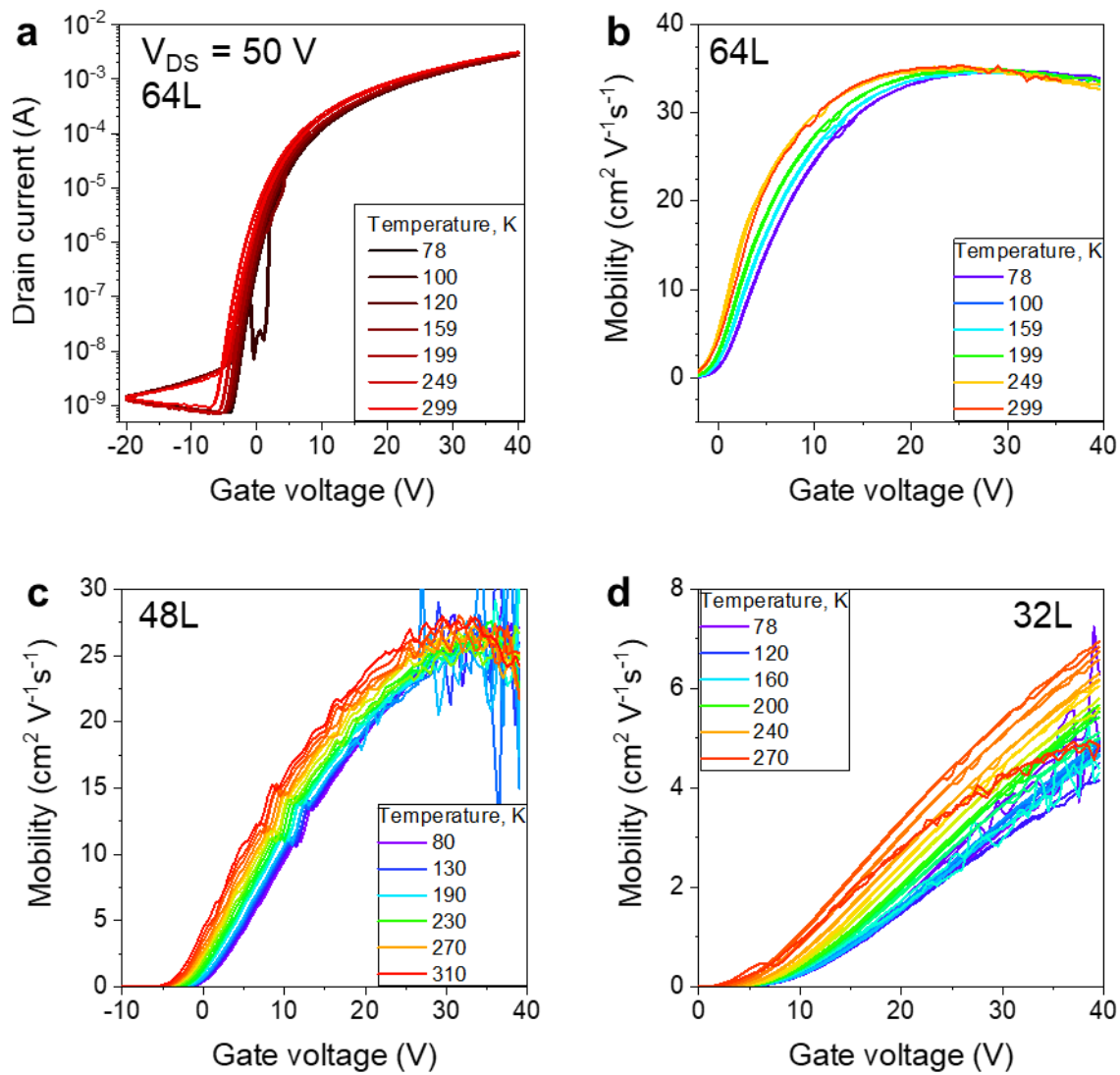
Figure S3. (a) Transfer characteristics of an In$_2$O$_3$ transistor of 15 nm thickness (corresponding to 64 sprayed layers or 64L), measured at temperatures between 78 and 299 K. The channel width and length are 300 and 80 µm, respectively. Linear mobility at different temperatures calculated from the transfer characteristic of TFTs of different thicknesses equivalent to (b) 64 layers, (c) 48 layers and (d) 32 layers.
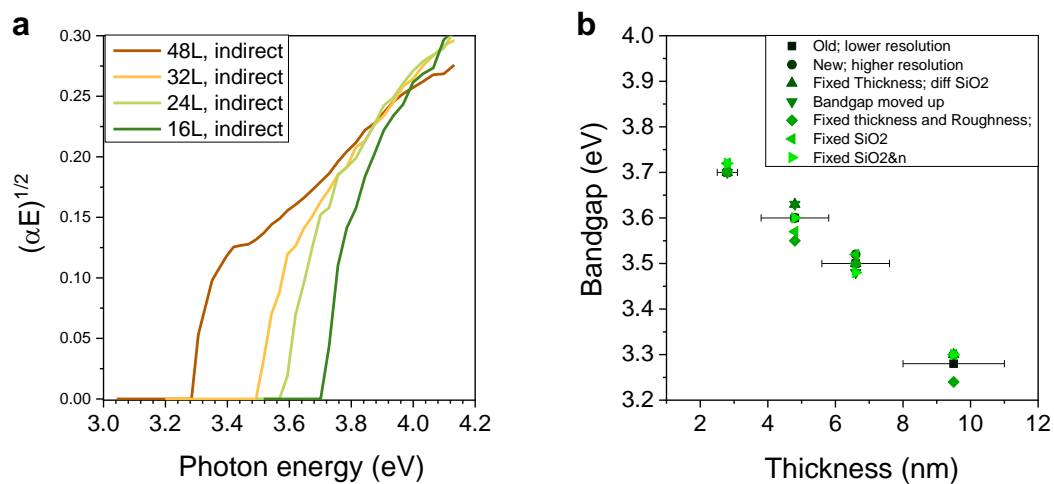
Figure S4. (a) Representative Tauc plots for In_2O_3 layers of different thicknesses, resulting from increasing numbers of sprayed layers, from 16 to 48. (b) Optical bandgap measured from Tauc plots as a function of thin film thickness calculated from the interpolation of the ellipsometric data using seven different computational models.
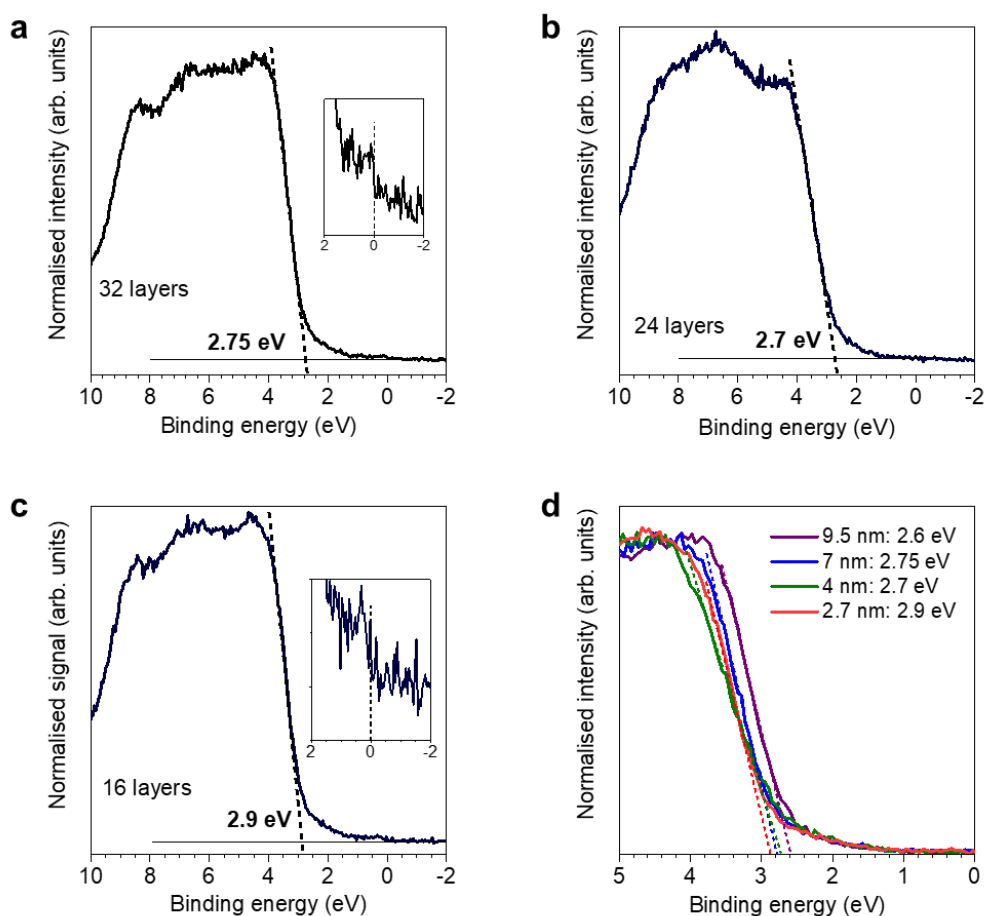
Figure S5. XPS measurements of spray deposited In_2O_3 thin films of different thicknesses, equivalent to (a) 32 sprayed layers, (b) 24 layers, (c) 16 layers. (d) Comparison between spectra of different thicknesses between 2.7 and 9.5 nm showing an intersection of a linear fit. For samples which exhibited a Fermi level (E_F) feature (a and c), the Fermi level features were used for binding energy alignment. No alignment was carried out for samples where no E_F feature was observed. However, since the samples had very little carbon impurities, the XPS equipment had an efficient charge compensation mode and the measurements were very reproducible, we were able to use the data as measured with a very low uncertainty. To normalise the graphs, we used the highest-energy valence band feature. To measure VBM from the intersection of a linear fit, we used a horizontal reference line based on the negative photoelectron energy spectrum (on the right of E_F feature in the graphs a-c).

a E

E_C

E_F

N_1

DoS

b

E_C

E_F

$N_2 > N_1$

c
$$R = \frac{\rho L}{Wt}$$

d
$$\frac{1}{\rho} = \sigma = N\mu e$$

e
$$N = \int g(E - E_F)f(E - E_F)dE$$

f
$$g(E - E_F) = N_0\sqrt{E_C - E_F}$$

g
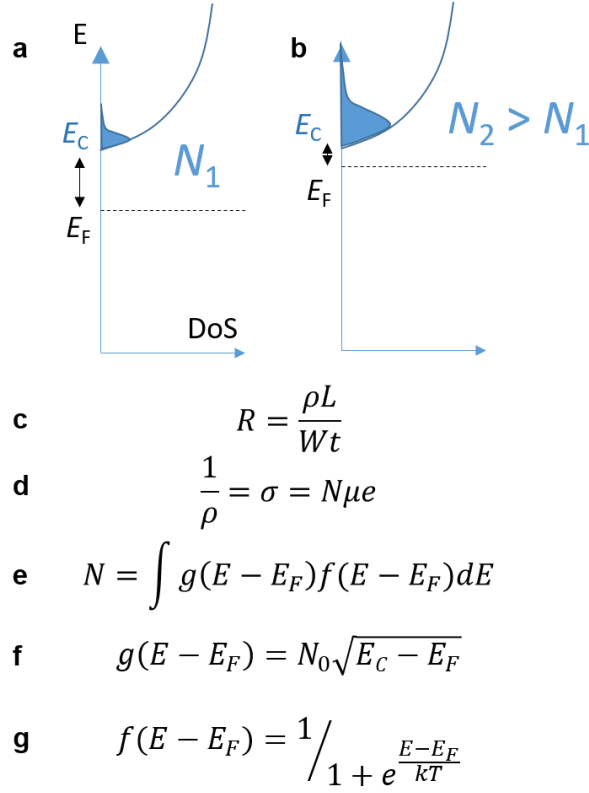$$f(E - E_F) = 1 \Big/ 1 + e^{\frac{E-E_F}{kT}}$$

Figure S6. Diagrammatic depiction of the method employed for conduction band offset calculation using the experimentally measured transistor resistance.[3] (a) and (b) a diagram showing electron occupation of the conduction band states: conduction band offset in (a) is larger than the one in (b), leading to a higher concentration of free carriers in (b), with the curve representing density of states (DoS). (c) Resistance R as a function of resistivity ρ, channel length L, width W and thickness t; (d) relation between resistivity, conductivity σ, carrier concentration N, electron mobility μ and electron charge e; (e) charge concentration as an integral of density of states $g(E)$ and Fermi-Dirac distribution $f(E)$; (f) three-dimensional density of states as a function of energy with N_0 being a material specific constant $\frac{1}{2\pi^2}\left(\frac{2m^*}{\hbar^2}\right)^{3/2}$, where m^* is effective electron mass and $\hbar$ is Planck constant; (g) Fermi-Dirac distribution.
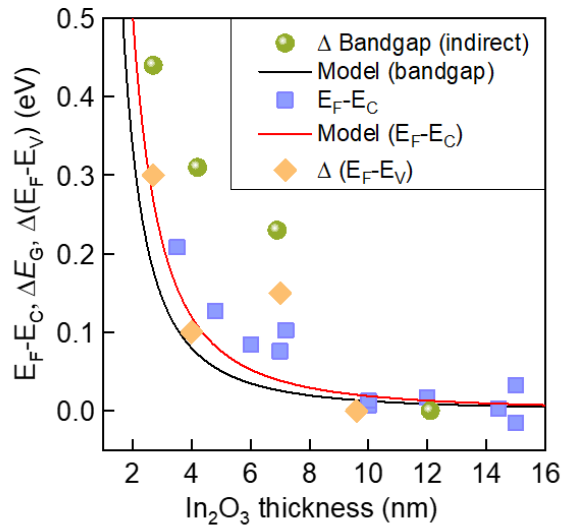
Figure S7. (c) Thickness dependence of the conduction band offset (E_F-E_C), the change in valence band offset (ΔE_F-E_V) and optical bandgap (ΔE_G) for In_2O_3 layers. The solid lines are a theoretical calculation for the energy shifts due to quantum confinement calculated using equation (3): the conduction band offset is calculated using only the effective electron, whereas the black line is calculated using the effective masses of both electron and hole for conduction band offset and valence band offset shifts, respectively. The energy differences were calculated by assuming as reference values those measured for the thickest In_2O_3 layers.
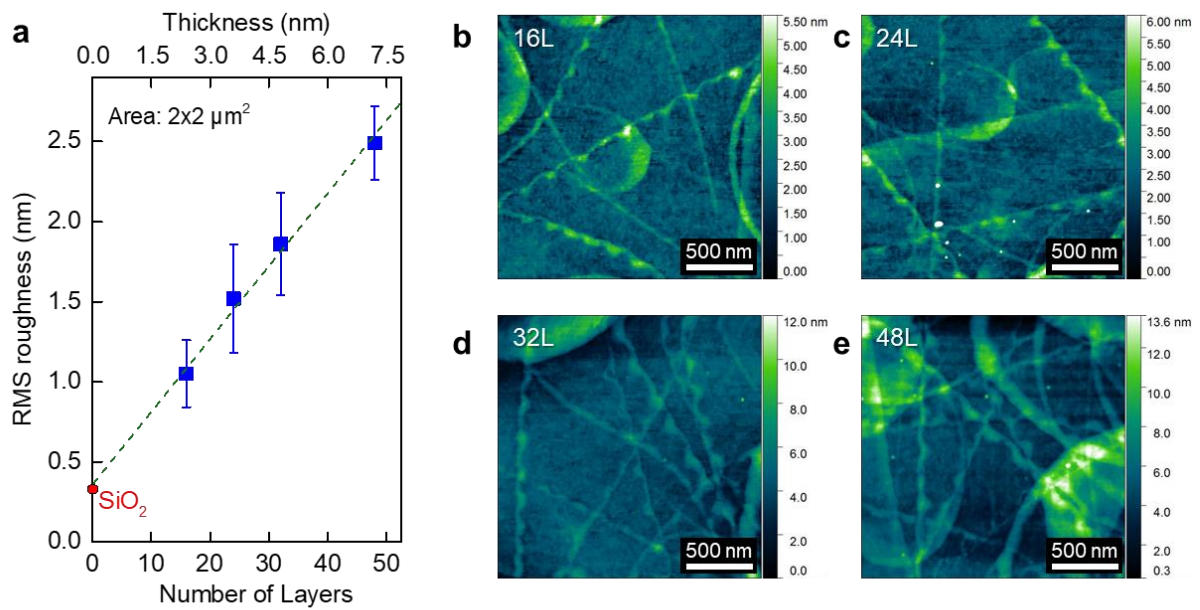
Figure S8. (a) Thickness dependence of the In_2O_3 films' RMS surface roughness derived from AFM images; (b-e) AFM topography images of In_2O_3 thin films with different thicknesses. The scan area is 2×2 μm^2 in all cases. The spherical features and visible lines in the surface topography are the result of intermittent precursor droplet interaction with the hot substrate surface during spray deposition (for the details of the growth process see Isakov *et al.*, in reference 26). The value on the top left corner of each image indicates the number of spraying layers, *i.e.* (b) 16 layers, (c) 24 layers, (d) 32 layers, and (e) 48 layers.
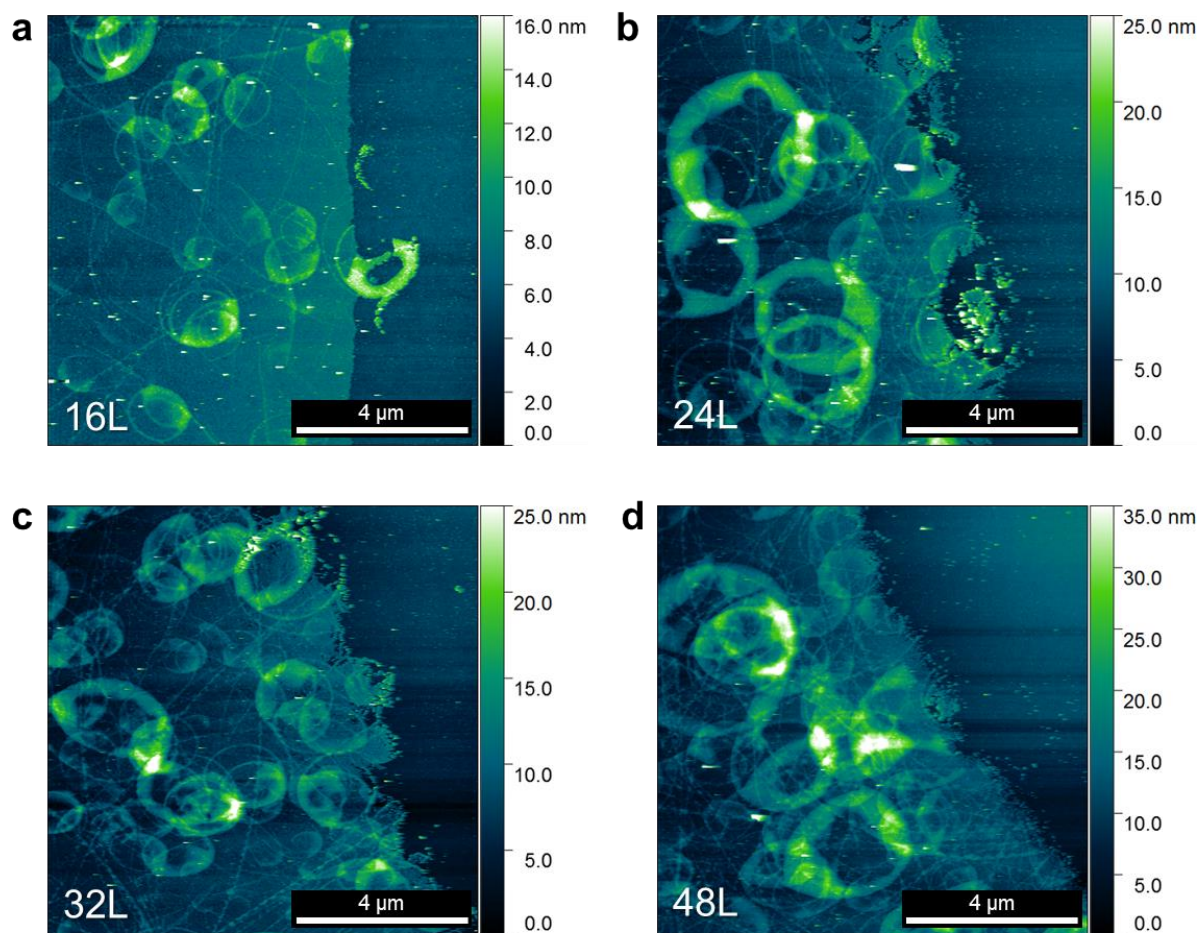
Figure S9. AFM topography images of the In$_2$O$_3$ thin films used for thickness measurements. The value on the bottom left corner of each image indicates the number of sprayed layers, *i.e.* (a) 16 layers, (b) 24 layers, (c) 32 layers and (d) 48 layers.
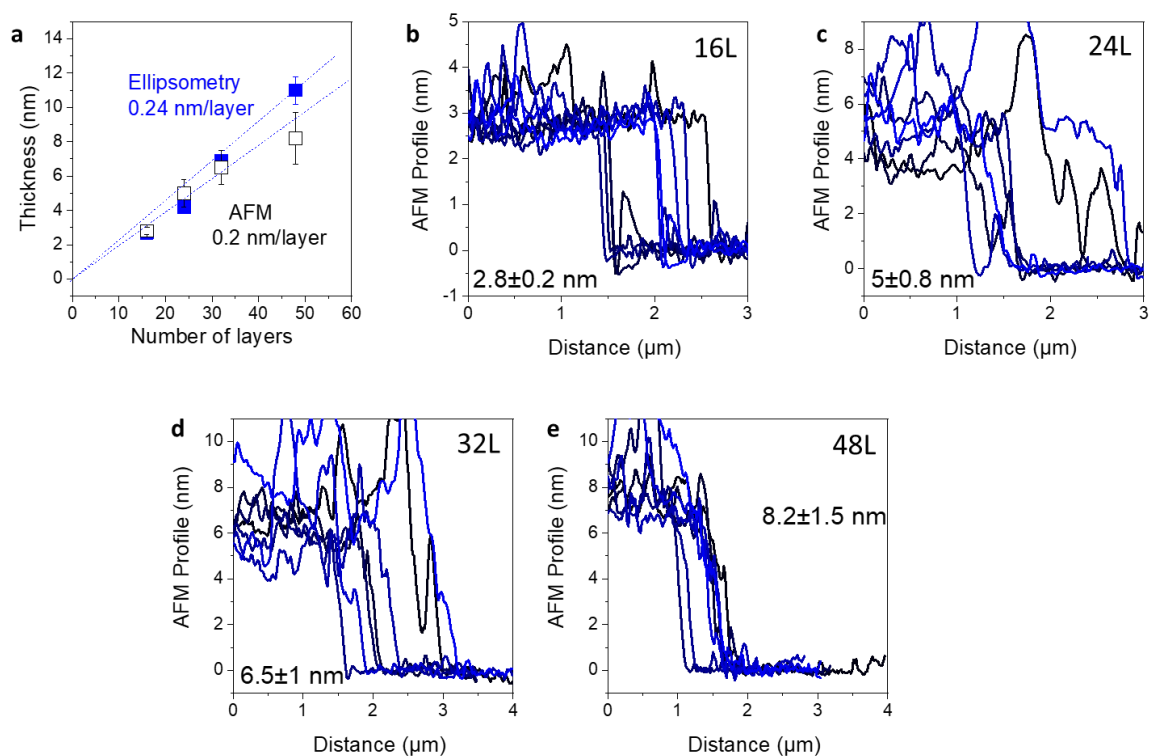
Figure S10. (a) Thickness of resulting In_2O_3 films as a function of the number of sprayed layers during the deposition, measured via ellipsometry (blue squares) or AFM (white squares). The dotted lines represent linear fits whose slope indicate the growth rate in nm per layer. (b-e) Step profiles extracted from AFM measurements shown in **Figure S9** for samples of different thicknesses. For each topography image, a multitude of profile lines were extracted and the mean and standard deviation values for the layer thickness was calculated from them. The numbers in the top right corners indicate the number of spraying layers during the spray pyrolysis deposition, *i.e.* (b) 16 layers, (c) 24 layers, (d) 32 layers and (e) 48 layers.
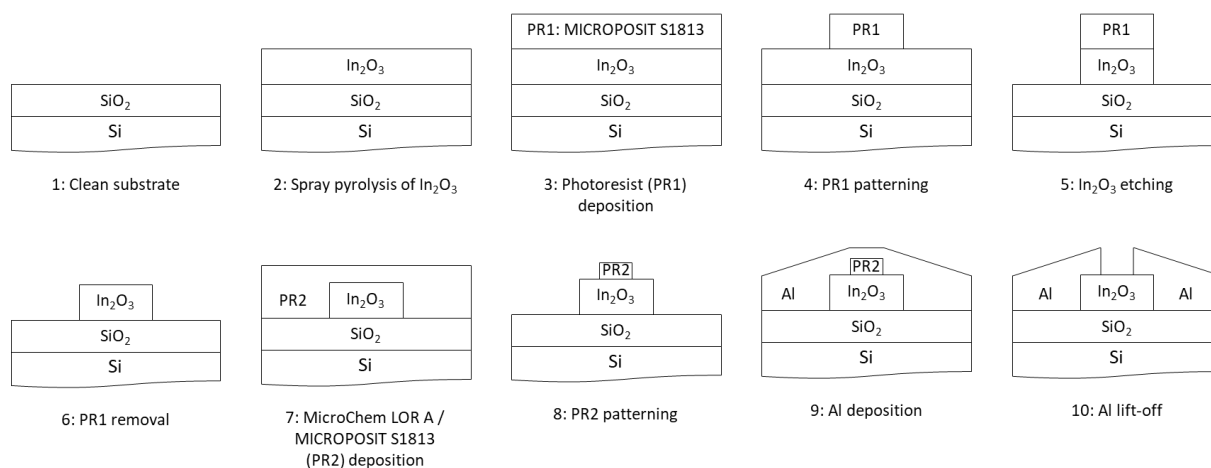
Figure S11. Schematic illustration of the various process used to fabricate the devices used for the 2pp and 4pp measurements. Material patterning was performed using conventional photolithography to etch the In_2O_3 layer and lift-off to pattern the top Al electrodes.

Supporting Information References

[1] W. L. Kalb, B. Batlogg, Phys. Rev. B 2010, 81, 035327.

[2] S. M. Skinner, J. Appl. Phys. 1955, 26, 498.

[3] S. M. Sze, K. K. Ng, *Physics of Semiconductor Devices*, John Wiley & Sons, Inc., 2006.